



Synthesis of stable monodisperse AuPd, AuPt, and PdPt bimetallic clusters encapsulated within LTA-zeolites



Trenton Otto^a, José M. Ramallo-López^b, Lisandro J. Giovanetti^b, Félix G. Requejo^b, Stacey I. Zones^c, Enrique Iglesia^{a,d,*}

^a Department of Chemical and Biomolecular Engineering, University of California at Berkeley, Berkeley, CA 94720, USA

^b Instituto de Investigaciones Físicoquímicas Teóricas y Aplicadas – INIFTA (CONICET, UNLP), 1900 La Plata, Argentina

^c Chevron Energy Technology Company, Richmond, CA 94804, USA

^d Division of Chemical Sciences, E.O. Lawrence Berkeley National Laboratory, Berkeley, CA 94720, USA

ARTICLE INFO

Article history:

Received 16 June 2016

Accepted 24 July 2016

Keywords:

Bimetallic catalyst

Noble metals

Sinter stable

Encapsulation

LTA zeolite

Hydrothermal synthesis

Oxidative dehydrogenation

ABSTRACT

AuPd, AuPt, and PdPt bimetallic clusters uniform in size and composition were prepared using hydrothermal assembly of LTA crystals around cationic precursors stabilized by protecting mercaptosilane ligands. The sulfur moiety in these bifunctional ligands forms adducts that prevent premature reduction or precipitation of metal precursors during crystallization. The silane groups can form bridges with silicate oligomers as they form, thus enforcing homogeneous distributions of precursors throughout crystals and ensuring that subsequent reductive treatments lead to the two elements residing within small and nearly monodisperse clusters. Their confinement within LTA crystals, evident from microscopy and titrations with large poisons, renders them stable against sintering during thermal treatments at high temperatures (820–870 K). Infrared spectra of chemisorbed CO show that bimetallic surfaces are free of synthetic debris after thermal treatments; these spectra also indicate that intracuster segregation occurs upon CO chemisorption, a demonstration of the presence of the two elements within the same clusters. The number and type of atoms coordinated to a given absorber atom, determined from the fine structure in X-ray absorption spectra, are consistent with bimetallic structures of uniform composition. The rates of ethanol oxidative dehydrogenation on these bimetallic clusters were essentially unaffected by exposure to dibenzothiophene, a large poison that suppresses rates on unconfined clusters, indicating that bimetallic clusters are protected within the confines of LTA crystals. These synthetic protocols seem generally applicable to other bimetallic compositions and zeolites, for which the monometallic counterparts have been successfully encapsulated within several microporous frameworks using ligand-stabilized precursors and hydrothermal crystallization methods.

© 2016 Elsevier Inc. All rights reserved.

1. Introduction

Bimetallic nanoparticles are useful as catalysts because of the unique electronic and structural features conferred by atomic mixing of two or more elements at the nanoscale. Such features, in turn, are consequential for turnover rates and selectivities in reactions as diverse as CO oxidation [1], alkane dehydrogenation [2], and NO_x reduction [3]. These bimetallic synergies also bring ancillary benefits [4]; a second metal can assist the reduction of another one [5], inhibit sintering during thermal treatments [6], or weaken the effects of site blocking by S-atoms or other titrants [7]. These

consequences may reflect ligand effects that cause one element to influence the electronic properties of another one [8] or ensemble effects caused by the dilution of monometallic domains [9]. The dissection of such effects into their causative components requires the synthesis of particles uniform in composition and size [9], an elusive objective because of the dearth of effective and general synthetic strategies.

Sequential adsorption and precipitation or co-impregnation of two metal salts onto mesoporous scaffolds [10] does not consistently place the component metals in atomic proximity [10], a challenge that can be addressed by sequential grafting of organometallic precursors onto supports [10]. Such grafting enforces metal-metal binding through covalent attachments between the first and second precursors deposited. The availability of precursors that prefer mutual interactions over those with the

* Corresponding author at: University of California, Berkeley, 103 Gilman Hall, Berkeley, CA 94720-1462, USA. Fax: +1 (510) 642 4778.

E-mail address: iglesia@berkeley.edu (E. Iglesia).

support limits the scope of such protocols, which often lead to the concurrent formation of monometallic clusters of the second precursor used in the sequence [10]. Galvanic displacement and electroless deposition, in contrast, selectively place a second metal into existing clusters of another metal via redox reactions [11]. Compositional uniformity in these methods requires seed clusters uniform in size and strategies to minimize homogeneous nucleation of the second component using solvents as reductants [9]. Colloidal synthesis methods involving the reduction of precursors in the presence of protecting polymers [11] can also form small clusters uniform in size and composition [9,12]; such uniformity, however, is frequently compromised by thermal treatments essential to deprotect the metal surfaces, as required for their catalytic function [9,11].

The nanometer-sized voids provided by crystalline zeolite frameworks can be used as containers for bimetallic clusters [11]. Their confinement within such voids allows the selection of certain reactants and transition states over others based on molecular size and the protection of active surfaces from large titrants and poisons by exploiting zeolite shape selectivity [13,14]. Confinement is often achieved by the exchange of solvated cationic precursors into the anionic zeolite frameworks [4]. Reductive treatments then form monometallic clusters, and the subsequent exchange and reduction of a second metal can form, in some instances, confined bimetallic clusters that are less prone to sintering than their monometallic counterparts [4]. Inhomogeneous cluster compositions, however, are often observed and such exchange methods require zeolite channels that allow the diffusion of the solvated cationic precursors and their charge-balancing double layer [11,15].

Here, we report an alternate route for the synthesis of small bimetallic clusters, uniform in size and composition, within LTA zeolite crystals, a framework with apertures too small to allow precursor exchange. We illustrate this general synthetic strategy for a range of AuPd, AuPt, and PdPt compositions. In doing so, we extend techniques that use protecting ligands to stabilize metal cation precursors against premature precipitation as colloidal metals of oxyhydroxides at the hydrothermal conditions required to crystallize zeolite frameworks [13,14]. Hydrothermal LTA crystallization in the presence of ligated precursors of two different elements leads to the formation of nearly monodisperse bimetallic clusters (1–2 nm); these clusters expose surfaces free of synthetic debris after sequential thermal treatments in O₂ and H₂, without compromising LTA crystallinity. The bimetallic nature of the clusters was shown by X-ray absorption spectroscopy and confirmed by the infrared spectra of chemisorbed CO. The protecting 3-mercaptopropyl-trimethoxysilane ligands prevent precipitation, reduction, and coalescence of the metals before the formation of LTA frameworks. These ligands also form siloxane bridges with silicate oligomers to enforce confinement and uniform placement of precursors throughout zeolite crystals, thus ensuring bimetallic mixing and the nucleation of small confined clusters, even after thermal treatments that remove the ligands and their S-atoms. The retention of these clusters within zeolite crystals was demonstrated from ethanol oxidation rates on samples exposed to dibenzothiophene, which would irreversibly poison any unconfined clusters [13].

2. Experimental methods

2.1. Reagents

HAuCl₄·3H₂O (99.999%, Sigma-Aldrich), Pd(NH₃)₄(NO₃)₂ (99.99%, Sigma-Aldrich), Pd(NH₃)₄Cl₂ (99.99%, Sigma-Aldrich), H₂PtCl₆ (8% wt. in H₂O, Sigma-Aldrich), 3-mercaptopropyl-trimethoxysilane (95%, Sigma-Aldrich), NaOH (99.99%, Sigma-Aldrich),

Ludox AS-30 colloidal silica (30% wt. suspension in H₂O, Sigma-Aldrich), NaAlO₂ (53% Al₂O₃, 42.5% Na₂O, Riedel-de Haën), mesoporous SiO₂ (Davisil, grade 646, surface area: 294 m² g⁻¹), fumed SiO₂ (Cab-O-Sil, HS-5, 310 m² g⁻¹), CaCl₂·2H₂O (EMD Millipore), acetone (99.9%, Sigma-Aldrich), ethanol (99.9%, Sigma-Aldrich), ethylenediamine (98%, Sigma-Aldrich), dibenzothiophene (98%, Sigma-Aldrich), air (extra dry; 99.999%, Praxair), H₂ (99.999%, Praxair), He (99.999%, Praxair), Ar (99.999%, Praxair), 25% O₂/He (99.999%, Praxair), and 1.0% CO/He (99.999%, Praxair) were used as received.

2.2. Materials synthesis

2.2.1. Synthesis of Au, Pd, Pt and AuPd, AuPt, and PdPt clusters within LTA crystals

Preparation procedures for bimetallic metal-encapsulated Na-LTA zeolites (M₁M₂NaLTA, where M₁ and M₂ are Au, Pd, or Pt) were adapted from hydrothermal synthesis protocols for monometallic systems [13,14]. Similar synthetic protocols were used for monometallic (AuNaLTA, PdNaLTA, PtNaLTA) and bimetallic (Au_nPd_{100-n}NaLTA, Au_nPt_{100-n}NaLTA, Pd_nPt_{100-n}NaLTA; *n* is the atomic percentage of the first element) samples. For example, Au₅₀Pd₅₀NaLTA was prepared by dissolving 3-mercaptopropyl-trimethoxysilane (0.96 g) and NaOH (4.8 g) in deionized H₂O (17.9 MΩ resistance; 18 cm³) in an open polypropylene bottle (125 cm³) using magnetic stirring (6.7 Hz; 8 h). Then, aqueous HAuCl₄·3H₂O (0.156 g in 9 cm³ deionized H₂O) and Pd(NH₃)₄(NO₃)₂ (0.118 g in 9 cm³ deionized H₂O) solutions were concurrently added dropwise to the ligand-NaOH solution over 0.5 h while stirring (6.7 Hz). Colloidal silica (10.67 g, Ludox AS-30) was then added, and the polypropylene bottle was capped and heated to 353 K for 0.5 h with continuous agitation (6.7 Hz). The bottle and its contents were then cooled to ambient temperature, and an aqueous solution of NaAlO₂ (6.0 g dissolved in 18 cm³ deionized H₂O at ambient temperature) was added dropwise while stirring (6.7 Hz, 2 h). This procedure formed a homogeneous synthesis gel with a molar composition of 1.7 SiO₂/1 Al₂O₃/3.2 Na₂O/110 H₂O/0.013 Au/0.013 Pd/0.156 ligand, which was heated to 373 K while stirring (6.7 Hz, 12 h) to form Au₅₀Pd₅₀NaLTA.

The solids formed were filtered (Pyrex 3606 fritted funnel, 4–5.5 μm), washed with deionized H₂O until the rinse liquids reached a pH of 7–8, and treated in ambient air within a convection oven at 373 K for 8 h. They were then heated in flowing dry air (1.67 cm³ g⁻¹ s⁻¹) from ambient temperature to 623 K (at 0.033 K s⁻¹) and held for 2 h, cooled to ambient temperature, and then heated to 623 K (at 0.033 K s⁻¹) in flowing H₂ (1.67 cm³ g⁻¹ s⁻¹) and held for 2 h. A final heating procedure in air (1.67 cm³ g⁻¹ s⁻¹) at 723 K (0.033 K s⁻¹) was then conducted for 2 h.

Bimetallic compositions were adjusted by varying the ratio of cationic precursors (HAuCl₄·3H₂O, Pd(NH₃)₄(NO₃)₂, H₂PtCl₆) in the gel, while maintaining the same nominal 1% wt. metal loading as in the monometallic samples. Six moles of 3-mercaptopropyl-trimethoxysilane were used per mole of metal for all compositions. The metal contents in all samples were measured by inductively coupled plasma optical emission spectroscopy (ICP-OES) using a Perkin Elmer 5300 DV optical emission ICP analyzer.

Metal-NaLTA samples (0.42 nm apertures, [13]) were exchanged with Ca²⁺ ions after O₂ and H₂ treatments to convert them to CaLTA (0.50 nm apertures, [14]) before CO chemisorption and infrared studies (Section 2.3.3). Na⁺ was exchanged for Ca²⁺ to widen the LTA apertures and allow more rapid diffusion of CO into the interior of the crystallites [14]. The exchange was performed by adding metal-NaLTA samples (1–5 g) to an aqueous solution of CaCl₂·2H₂O (1 M; 100 cm³/g zeolite) and stirring (6.7 Hz, 8 h) at ambient temperature. This procedure was repeated ten times to ensure full Ca²⁺ exchange [14]. The solids were finally filtered

and washed with deionized water ($1500 \text{ cm}^3 \text{ g}^{-1}$) and treated in a convection oven at 373 K for 12 h before their use in infrared studies.

2.2.2. Synthesis of Au, Pd, and Pt clusters on mesoporous SiO_2

Au, Pd, and Pt clusters dispersed on mesoporous SiO_2 were synthesized and used as oxidative dehydrogenation (ODH) catalysts (Sections 2.3.5 and 3.5) for comparison with the bimetallic clusters supported by zeolites. Pd/ SiO_2 and Pt/ SiO_2 catalysts were prepared with incipient wetness impregnation using aqueous solutions of Pd $(\text{NH}_3)_4\text{Cl}_2$ and H_2PtCl_6 , respectively. These silica-supported clusters were treated in ambient air, flowing dry air, and flowing H_2 using the same procedures as the metal-zeolite samples (Section 2.2.1).

Au clusters dispersed on SiO_2 (Cab-O-Sil, HS-5, $310 \text{ m}^2 \text{ g}^{-1}$) were prepared using an $\text{Au}(\text{en})_2\text{Cl}_3$ (en = ethylenediamine) complex previously shown to lead to small clusters [14,16]. Experimental procedures detailing the synthesis of the $\text{Au}(\text{en})_2\text{Cl}_3$ complex and Au/ SiO_2 can be found in the Supporting Information (SI) (Section S1).

2.3. Characterization of zeolite structures and embedded metal clusters

2.3.1. Powder X-ray diffraction

X-ray diffractograms (XRD) were used to confirm LTA zeolite crystallinity and the absence of large (>10 nm) metal clusters. Diffractograms were measured with a D8 Discover GADDS Powder Diffractometer with Cu $K\alpha$ radiation ($\lambda = 0.15418 \text{ nm}$, 40 kV, 40 mA) at 2θ values from 5° to 50° and a scan rate of $0.00625^\circ \text{ s}^{-1}$. The samples were ground into fine powders and placed and leveled on quartz slides for these measurements.

2.3.2. Transmission electron microscopy

Transmission electron micrographs (TEM) were collected with a Philips/FEI Tecnai 12 microscope at 120 kV by dispersing finely ground powders in acetone and then onto holey carbon films supported on 400 mesh copper grids (Ted Pella Inc.). Metal cluster size distributions were measured from >300 particles for each sample, and used to determine surface-averaged cluster diameters $\langle d_{\text{TEM}} \rangle$ [13]:

$$\langle d_{\text{TEM}} \rangle = \frac{\sum n_i d_i^3}{\sum n_i d_i^2} \quad (1)$$

where n_i is the number of clusters with diameter d_i . These size distributions were further used to calculate dispersity index (DI) values, which are given by the ratio of the surface-averaged ($\langle d_{\text{TEM}} \rangle$) to the number-averaged ($\langle d_n \rangle$) diameter [13]:

$$\text{DI} = \frac{\langle d_{\text{TEM}} \rangle}{\langle d_n \rangle} = \frac{\left(\frac{\sum n_i d_i^3}{\sum n_i d_i^2} \right)}{\left(\frac{\sum n_i d_i}{\sum n_i} \right)} \quad (2)$$

These DI values provide the accepted metric of size uniformity, with values smaller than 1.5 taken as evidence of excellent monodispersity [17]; they are seldom reported, in spite of IUPAC guidance [9], leading us to also report here standard deviations as a less rigorous measure of size uniformity.

Metal dispersions (D), defined as the fraction of metal atoms exposed at cluster surfaces, were estimated from $\langle d_{\text{TEM}} \rangle$ [17] as follows:

$$D = 6 \frac{\bar{v}_m / \bar{a}_m}{\langle d_{\text{TEM}} \rangle} \quad (3)$$

where \bar{v}_m is the effective bulk atomic density of the bimetallic samples, estimated as the composition-weighted average of the v_m values for pure Au ($16.49 \times 10^{-3} \text{ nm}^3$), Pd ($14.70 \times 10^{-3} \text{ nm}^3$), or Pt

($15.10 \times 10^{-3} \text{ nm}^3$) [17]. The value of \bar{a}_m , the effective area occupied by a metal atom on polycrystalline surfaces, was also calculated as a composition-weighted mean from the pure component values (Au: $8.75 \times 10^{-2} \text{ nm}^2$, Pd: $7.93 \times 10^{-2} \text{ nm}^2$, Pt: $8.07 \times 10^{-2} \text{ nm}^2$) [17].

2.3.3. Infrared spectra of chemisorbed CO on metal-LTA zeolites

Infrared (IR) spectra of CO chemisorbed on metal-CaLTA wafers (40 mg cm^{-2}) were used to probe the surface composition of bimetallic clusters. IR spectra were acquired using a Thermo Nicolet 8700 spectrometer equipped with an in situ flow cell. All sample wafers were first heated in flowing 20% H_2/He mixtures ($42.0 \text{ cm}^3 \text{ g}^{-1} \text{ s}^{-1}$) from ambient temperature to 573 K (0.033 K s^{-1}) for 1 h. Pd_nPt_{100-n}CaLTA samples were then cooled rapidly in He flow ($42.0 \text{ cm}^3 \text{ g}^{-1} \text{ s}^{-1}$) to 313 K (-0.17 K s^{-1}), and exposed to flowing CO/He ($42.0 \text{ cm}^3 \text{ g}^{-1} \text{ s}^{-1}$; 1.0 kPa CO) before collecting IR spectra. Au_nPd_{100-n}CaLTA samples were instead cooled to 278 K (-0.17 K s^{-1}) in flowing He ($42.0 \text{ cm}^3 \text{ g}^{-1} \text{ s}^{-1}$) after the H_2/He treatment at 573 K, before collecting spectra in flowing CO/He ($42.0 \text{ cm}^3 \text{ g}^{-1} \text{ s}^{-1}$; 1.0 kPa CO). The Au_nPd_{100-n}CaLTA samples were then heated in this flowing CO/He to 353 K (0.033 K s^{-1}) for 0.5 h, and then cooled back to 278 K (-0.17 K s^{-1}) under continuous CO flow for a second spectra to be collected. Au_nPt_{100-n}CaLTA samples were treated analogously to Au_nPd_{100-n}CaLTA, except they were cooled to 263 K instead of 278 K. The AuPd and AuPt bimetallic samples were subjected to this intermittent period of CO exposure and heating with the intent of inducing changes in the surface compositions of alloyed clusters (Section 3.3). Spectral contributions from CO(g) and Ca²⁺-CO complexes [14] were subtracted from all reported spectra.

2.3.4. X-ray absorption spectroscopy and analysis of the extended X-ray absorption fine structure

X-ray absorption spectra (XAS) were acquired in transmission mode at the Au-L₃ edge (11,919 eV) [18], the Pd-K edge (24,350 eV) [18], and the Pt-L₃ edge (11,564 eV) [18] using the XDS and XAFS-2 beamlines of the LNLS (Laboratório Nacional do Luz Síncrotron, Campinas, Brazil). Two monochromators were used as follows: a Si(3 1 1) crystal for the Pd-K edge and a Si(1 1 1) crystal for the Pt-L₃ and Au-L₃ edges. Intensities were measured using three sequential ionization chambers filled with mixtures of N₂ and Ar at ambient temperature and 1 bar of pressure. Photon energies were calibrated using a thin metal film (Au, Pd, or Pt) placed between the second and third ionization chambers. XAS spectra were measured for Au₅₀Pd₅₀NaLTA and Pd₆₅Pt₃₅NaLTA samples. Spectra were collected at the absorption edge for each metal present in a range between 200 eV before and 1000 eV after each edge. The samples (0.1 g each) were treated in 10% H_2/Ar flow ($1.67 \text{ cm}^3 \text{ g}^{-1} \text{ s}^{-1}$) at 573 K (0.033 K s^{-1}) for 1 h and cooled to ambient temperature under Ar flow ($1.67 \text{ cm}^3 \text{ g}^{-1} \text{ s}^{-1}$). They were then transferred in an Ar blanket to a cell sealed hermetically with Kapton® windows. The samples were stored in this cell for ~10 h, after which the XAS spectra were collected at ambient temperature.

The extended X-ray absorption fine structure (EXAFS) data were analyzed using the IFEFFIT package (Athena, Artemis) [19]. The coordination numbers (N), interatomic distances (D), and Debye-Waller factors (σ^2) were obtained from nonlinear regressions of the Fourier transformed data implemented in Artemis [19]. Simulated amplitudes and phase shifts for all single scattering paths were obtained using the FEFF code [20]. These modeled scattering paths were calculated using crystallographic structures of either monometallic lattices (for Au-Au, Pd-Pd, and Pt-Pt paths) or mixed phase lattices (for Pd-Au and Pd-Pt paths) [21–23]. EXAFS data extracted from bimetallic samples were fit simultaneously at both metal edges, ensuring consistency in the D and σ^2 values. Single scattering by O and S atoms, with theoretical amplitudes and

phases calculated from metal oxide (PdO, PtO) [24,25] or metal sulfide (PdS, PTS, Au₂S₃) [26–28] crystal structures, was also included in the fits to determine whether metal oxide or metal sulfide species were present. Passive reduction factors [19] for each metal (Au: 0.95, Pd: 0.83, Pt: 0.96) were obtained from fits to the EXAFS spectra of the metal foils by constraining the average coordination number of the first shell to 12.

2.3.5. Catalytic assessment of reactivity and encapsulation

Ethanol oxidative dehydrogenation (ODH) turnover rates were measured on catalyst powders first diluted 10-fold by mass with fumed SiO₂ (Cab-O-Sil, HS-5, 310 m² g⁻¹) and then pressed into pellets and sieved to retain 180–250 μm aggregates. These diluted samples were then mixed with 180–250 μm acid-washed quartz granules (1:1 mass) to prevent any temperature gradients caused by exothermic ODH reactions. Catalysts were placed on a porous quartz frit within a quartz tube (10 mm O.D.). Samples were heated in 20% O₂/He (1.67 cm³ g⁻¹ s⁻¹) from ambient temperature to 393 K (at 0.033 K s⁻¹) and held at that temperature for rate measurements. Liquid ethanol and deionized water were vaporized into flowing O₂/He streams at 393 K using liquid syringe pumps (Cole Parmer, 60061 Series). He and O₂ flow rates were adjusted with mass flow controllers (Porter Instrument) to achieve the desired pressures (4 kPa alkanol, 9 kPa O₂, 87.5 kPa He, and 0.5 kPa H₂O). H₂O forms as an ODH product, and can have a co-catalytic effect; it was therefore added to maintain a constant concentration of all species throughout the catalyst bed, thus ensuring differential conditions. Alkanol conversions were kept below 5% and transfer lines were heated to 393 K to avoid condensation.

Turnover rates are defined as the molar ethanol conversion rates per surface metal atom estimated from the dispersion values defined in Eq. (3). Product formation was not detectable on NaLTA, fumed silica, or empty reactors. Turnover rates were extrapolated to the start of each experiment. Effluent concentrations were measured by gas chromatography (Shimadzu GC-2014) using a methyl-silicone capillary column (HP-1; 50 m × 0.32 mm, 1.05 μm film thickness) and a flame ionization detector.

Metal-NaLTA samples were exposed ex-situ to dibenzothio- phene (DBT), an organosulfur poison that irreversibly titrates noble metal surfaces [29], before their use in ethanol ODH reactions. Ex-situ treatments exposed metal-NaLTA and metal-SiO₂ samples to DBT dissolved in liquid ethanol (300 cm³ g⁻¹; DBT/metal molar ratio of 6) at ambient temperature for 4 h with magnetic agitation (6.7 Hz). The samples were then filtered and treated in ambient air at 343 K for 12 h, and used in ethanol ODH reactions at 393 K. Control samples were also prepared through an identical procedure but without DBT and used for ethanol ODH.

Ethanol (0.40 nm kinetic diameter, [13]), but not DBT (0.9 nm, [30]), can diffuse through the apertures of NaLTA (0.42 nm, [13]); thus, the extent of deactivation caused by exposure to DBT provides an assessment of the fraction of metal surfaces that are confined within zeolite crystals and therefore protected from any large molecules present in the extracrystalline fluid [13]. A comparison of rates before and after exposure to DBT on metal-NaLTA and metal-SiO₂ samples would then indicate the fraction of the active surfaces present at extracrystalline locations and thus the selectivity of the encapsulation.

3. Results and discussion

3.1. Metal content and phase purity of metal-LTA samples

LTA-encapsulated metal nanoparticles were synthesized with Au-Pd compositions (Au_nPd_{100-n}NaLTA), Au-Pt (Au_nPt_{100-n}NaLTA), or Pd-Pt (Pd_nPt_{100-n}NaLTA) and a broad range of atomic ratios

and a 1% wt. metal content (nominal; based on amounts of reagents used). The measured elemental compositions reported in Table 1 confirm the essentially complete incorporation of the metal precursors into the final product. These data indicate that the ability of the ligands to bind to the metal cations through the S-atoms and to the crystallizing framework through covalent siloxane bridges favors metal incorporation into the solids instead of their retention within the supernatant liquid that is removed by filtration after synthesis.

X-ray diffractograms of all samples (Fig. 1) after thermal treatment in O₂ (623 K) and then H₂ (623 K) (Section 2.2) detected the intended LTA crystals (>95% crystallinity; from integrated intensities of the three most intense Na-LTA lines). No diffraction lines for metal phases (Au, Pd, or Pt) were evident after treatment at 823 K and the LTA crystallinity was unaffected by thermal treatments in O₂ or H₂ even at 823 K. These data show that samples are crystalline, thermally stable, and free of large metal crystallites (>10 nm), which would have been evident in the diffractograms even at 1% wt. metal contents.

3.2. Assessment of cluster size distributions and thermal stability

Transmission electron micrographs were used to assess the size and infer the location and thermal stability of the metal structures formed during hydrothermal zeolite crystallization and subsequent thermal treatments in O₂ and H₂ (Section 2.2). For the respective monometallic systems (Au, Pd, Pt), previous studies have shown that these synthetic protocols lead to highly dispersed clusters free of synthetic debris and preferentially located within LTA or MFI crystals [13,14]. Metal clusters form via ligand removal and reduction of mononuclear cationic species that migrate within LTA crystals and deposit at locations where nuclei first form [13,14]. Their ultimate size depends on the mobility of these species during their reduction, causing higher H₂ treatment temperatures to form larger clusters [14]. These clusters, incipiently formed by treatments in H₂, are stabilized by the local enclosures provided by the zeolite framework and thus maintain their sizes even after subsequent thermal treatments in O₂ or H₂ at even higher temperatures [13,14]. Fig. 2 shows electron micrographs and size distributions for the monometallic clusters and for select bimetallic clusters in LTA. Table 1 reports TEM-derived surface-averaged

Table 1

Metal loadings, surface averaged particle diameters, metal compositions, and particle dispersity indices of metal-zeolite and metal-SiO₂ samples.

Sample	% wt. Metal ^a	Metal ratio ^a	$\langle d_{\text{TEM}} \rangle$ (nm) ^b	DI ^c
AuNaLTA	1.1	–	2.3 ± 0.4	1.09
PdNaLTA	1.0	–	1.6 ± 0.3	1.10
PtNaLTA	1.1	–	1.3 ± 0.3	1.17
Au ₆₇ Pd ₃₃ NaLTA	1.0	65 Au: 35 Pd	1.7 ± 0.3	1.09
Au ₅₀ Pd ₅₀ NaLTA	0.9	54 Au: 46 Pd	1.5 ± 0.3	1.08
Au ₃₃ Pd ₆₇ NaLTA	0.7	32 Au: 68 Pd	1.5 ± 0.3	1.11
Au ₆₇ Pt ₃₃ NaLTA	1.1	62 Au: 38 Pt	1.4 ± 0.3	1.15
Au ₅₀ Pt ₅₀ NaLTA	0.8	52 Au: 48 Pt	1.4 ± 0.3	1.09
Au ₃₃ Pt ₆₇ NaLTA	1.2	62 Au: 38 Pt	1.3 ± 0.2	1.07
Pd ₈₀ Pt ₂₀ NaLTA	1.1	80 Pd: 20 Pt	1.4 ± 0.3	1.09
Pd ₅₀ Pt ₅₀ NaLTA	1.0	56 Pd: 44 Pt	1.5 ± 0.3	1.08
Pd ₆₅ Pt ₃₅ NaLTA	1.1	61 Pd: 39 Pt	1.3 ± 0.2	1.06
Pd ₂₀ Pt ₈₀ NaLTA	1.0	24 Pd: 76 Pt	1.3 ± 0.2	1.05
Au/SiO ₂	2.2	–	2.7 ± 0.5	1.06
Pd/SiO ₂	0.6	–	3.1 ± 0.8	1.18
Pt/SiO ₂	0.8	–	2.4 ± 0.7	1.16

^a Analyzed by inductively coupled plasma optical emission spectroscopy (Section 2.2.1).

^b Surface area weighted mean cluster diameter determined via TEM (Section 2.3.2).

^c Dispersity Index computed as the surface averaged cluster diameter divided by the number averaged diameter (Section 2.3.2).

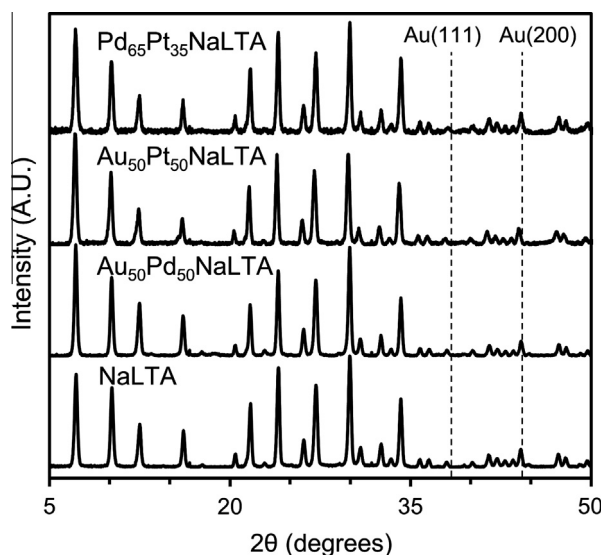


Fig. 1. XRD patterns of bimetallic metal-zeolite samples (Section 2.3.1). Total metal content in each sample is ~1% wt., except for the metal-free NaLTA standard.

cluster diameters ($\langle d_{\text{TEM}} \rangle$; Eq. (1)) and dispersity indices (DI; Eq. (2)) for each of the $\text{Au}_n\text{Pd}_{100-n}\text{NaLTA}$, $\text{Au}_n\text{Pt}_{100-n}\text{NaLTA}$, and $\text{Pd}_n\text{Pt}_{100-n}\text{NaLTA}$ samples synthesized by the protocols developed in this study. Similar to their monometallic counterparts, the clusters in these bimetallic samples are located predominantly within the zeolite crystallites, as we independently confirm here (Section 3.5) by exploiting shape selectivity conferred by confinement.

Surface-averaged diameters for monometallic samples (AuNaLTA : 2.3 nm, PdNaLTA : 1.6 nm, PtNaLTA : 1.3 nm; Table 1) vary inversely with the Tamman temperature [31] of each metal (Au: 668 K, Pd: 914 K, Pt: 1022 K), consistent with an inverse link between cohesive energies and the tendency to form the mobile species that mediate cluster growth. Each bimetallic sample gave a surface-averaged cluster size similar to that of the component with the higher Tamman temperature (e.g. $\text{Au}_{50}\text{Pd}_{50}\text{NaLTA}$: 1.5 nm, $\text{Au}_{50}\text{Pt}_{50}\text{NaLTA}$: 1.4 nm, and $\text{Pd}_{65}\text{Pt}_{35}\text{NaLTA}$: 1.3 nm; Table 1), indicating that the more mobile metal atoms are scavenged and rendered less mobile by the higher-melting metal. These bimetallic samples showed size distributions that were both unimodal (Fig. 2) and monodisperse (DI: 1.05–1.15; Table 1). Bimetallic clusters that are heterogeneously distributed in composition would typically show a broad range of cluster sizes because clusters rich in the less stable species tend to form larger agglomerates [31]. The small cluster diameters and monodisperse size distributions (i.e. $\text{DI} < 1.5$) of these bimetallic clusters in LTA zeolites, therefore, suggest the predominant presence of nanoparticles of uniform compositions.

The size and compositional uniformity of clusters in Au-containing samples (AuNaLTA , $\text{Au}_n\text{Pd}_{100-n}\text{NaLTA}$, and $\text{Au}_n\text{Pt}_{100-n}\text{NaLTA}$) was also probed via their UV–visible spectra. Monometallic Au clusters and core–shell structures with Au shells show localized surface plasmon resonance (LSPR, [32]) features at 500–600 nm [9], but monometallic Pt and Pd clusters or mixed Au–Pd and Au–Pt clusters do not [9]. Consequently, an LSPR band diagnoses the presence of Au clusters larger than the minimum size (2 nm diameter) required for detectable plasmon resonance [32]. AuNaLTA and physical mixtures of AuNaLTA with PdNaLTA or PtNaLTA exhibited LSPR bands, but $\text{Au}_n\text{Pd}_{100-n}\text{NaLTA}$ and $\text{Au}_n\text{Pt}_{100-n}\text{NaLTA}$ did not (Section S2, SI), confirming the absence of monometallic Au clusters >2 nm in diameter in these bimetallic samples.

Previous studies have shown that the confining environment within LTA crystals inhibits agglomeration of Pt and Pd clusters

during thermal treatments in air up to 873 K [13]; monometallic Au clusters in LTA and MFI are similarly stabilized by confinement, but start to sinter at slightly lower temperatures (823 K) than Pt or Pd [14]. The thermal stability of Au, Au–Pt and Au–Pd clusters was examined and compared here to determine whether the addition of Pd or Pt could improve the thermal stability of Au clusters. Such stability was probed with thermal treatments in flowing air to temperatures between 623 K and 873 K (at 0.033 K s^{-1}) for 5 h. TEM-derived surface-averaged cluster diameters ($\langle d_{\text{TEM}} \rangle$; Eq. (1)) for AuNaLTA , $\text{Au}_{50}\text{Pd}_{50}\text{NaLTA}$, and $\text{Au}_{50}\text{Pt}_{50}\text{NaLTA}$ are shown in Fig. 3 as a function of treatment temperature. Cluster diameters (AuNaLTA : 2.3 nm, $\text{Au}_{50}\text{Pd}_{50}\text{NaLTA}$: 1.5 nm, $\text{Au}_{50}\text{Pt}_{50}\text{NaLTA}$: 1.4 nm) were unaffected by thermal treatments up to 773 K. AuNaLTA sintered significantly after treatment at 873 K (3.8 nm), but bimetallic clusters grew only slightly (to 1.8 nm for $\text{Au}_{50}\text{Pd}_{50}$ and 1.6 nm for $\text{Au}_{50}\text{Pt}_{50}$) after similar protocols. In the same manner, the dispersity index (DI; Eq. (2)) increased significantly for AuNaLTA (1.07–1.62) after treatment at 873 K, but much less for bimetallic clusters ($\text{Au}_{50}\text{Pd}_{50}\text{NaLTA}$: 1.09–1.23, $\text{Au}_{50}\text{Pt}_{50}\text{NaLTA}$: 1.09–1.17), which remained essentially monodisperse ($\text{DI} < 1.5$) [17]. We surmise that the presence of Pd or Pt stabilizes Au species, thus decreasing their mobility at these temperatures and leading to greater size stability than in the case of pure Au clusters. These bimetallic effects, combined with the size stability conferred by confinement within microporous crystals [13,14], led to cluster sizes and thermal stabilities unattainable for metal or bimetallic clusters dispersed on mesoporous supports [13,14].

3.3. Infrared evidence for bimetallic clusters and for intracuster atomic mobility

Bimetallic clusters are typically described by heuristic constructs based on core–shell arrangements, ordered intermetallic compounds, or randomly mixed elements [33]. Such structures are perturbed through intracuster atomic mobility in response to the binding of molecules [9], to entropy effects that prevail at higher temperatures [34], or to interactions with a support [35]. Such processes require, however, that the two components reside within the same clusters, making changes in surface composition induced by adsorbed species a rigorous indicator of the presence of the two components within the same cluster. Here, we exploit these phenomena by measuring temporal changes in the infrared spectra of chemisorbed CO in order to determine surface compositions and their dynamic response to adsorbate-induced intracuster restructuring.

Infrared spectra of chemisorbed CO were acquired on the monometallic and bimetallic samples prepared as described in Section 2.2. The NaLTA hosts (0.42 nm apertures, [14]) were exchanged with Ca^{2+} to form CaLTA (0.50 nm apertures, [14]) before these measurements to allow rapid diffusion of CO at the sub-ambient temperatures required for the slow intracuster atomic diffusion needed to measure a transient response [9,14]. $\text{Au}_n\text{Pd}_{100-n}\text{CaLTA}$ and $\text{Au}_n\text{Pt}_{100-n}\text{CaLTA}$ bimetallic samples were first treated in H_2 (20 kPa) at 573 K for 1 h and cooled in He flow to sub-ambient temperatures (278 K and 263 K, respectively) before exposure to CO(g) (1 kPa) and infrared measurements (Section 2.3.3). This treatment leads to surfaces devoid of adsorbed species, thus favoring surface enrichment by Au, the component with the lower surface energy [9,36]. Spectra were collected after exposure to CO(g) and samples were then heated to 353 K in 1.0 kPa CO for 0.5 h and cooled back to 278 K or 263 K to acquire additional infrared spectra. The binding energy of CO on Pt (atop: 136 kJ mol^{-1} , [37]) or Pd (atop: 94 kJ mol^{-1} ; bridged: 146 kJ mol^{-1} , [37]) is stronger than that on Au (atop: 50 kJ mol^{-1} , [38]). Consequently, exposure of bimetallic particles to CO at temperatures that allow intraparticle atomic mobility would cause the return of Pt or

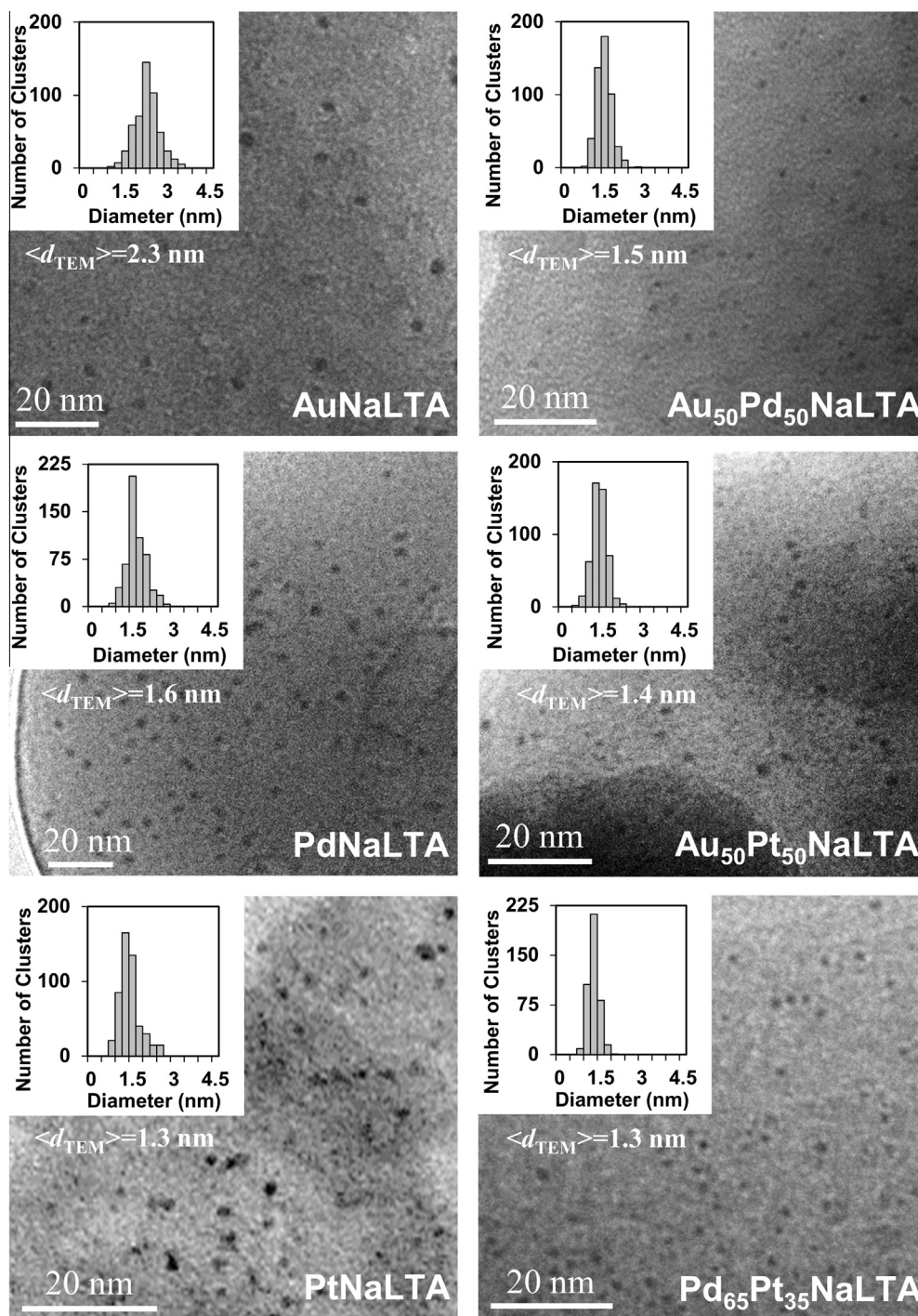


Fig. 2. Transmission electron micrographs, surface-averaged diameters, $\langle d_{\text{TEM}} \rangle$ (Eq. (1)), and diameter distributions for monometallic and bimetallic metal-zeolite samples. The metal content in each sample is $\sim 1\%$ wt.

Pd to cluster surfaces and to stronger infrared bands than after the initial exposure to CO at these low temperatures. Any differences in the infrared spectra before and after these heating cycles in the presence of CO(g) would indicate the presence of bimetallic clusters in $\text{Au}_n\text{Pd}_{100-n}\text{CaLTA}$ and $\text{Au}_n\text{Pt}_{100-n}\text{CaLTA}$. Such hysteresis is expected to be much weaker for $\text{Pd}_n\text{Pt}_{100-n}\text{CaLTA}$ samples, because of the similar CO binding energies on Pt and Pd. Bimetallic mixing in $\text{Pd}_n\text{Pt}_{100-n}\text{CaLTA}$ was confirmed by combining infrared (Section 3.3.3) and EXAFS (Section 3.4.2) methods.

3.3.1. Infrared spectra of chemisorbed CO on $\text{Au}_n\text{Pt}_{100-n}\text{CaLTA}$

The infrared spectra of CO chemisorbed on 1% wt. (metal) $\text{Au}_n\text{Pt}_{100-n}\text{CaLTA}$ ($n = 0, 33, 50, 67,$ and 100), measured in the presence of 1.0 kPa CO at 263 K before and after treatment in CO at 353 K, are shown in Fig. 4. Monometallic Au and Pt samples exhibit absorption bands at 2120 cm^{-1} and 2070 cm^{-1} respectively, corresponding to atop CO species on Au and Pt [14,39]. Bands for bridge-bonded CO on monometallic Pt ($1800\text{--}1900 \text{ cm}^{-1}$, [40,41]) are too weak for accurate quantitation of their intensity or

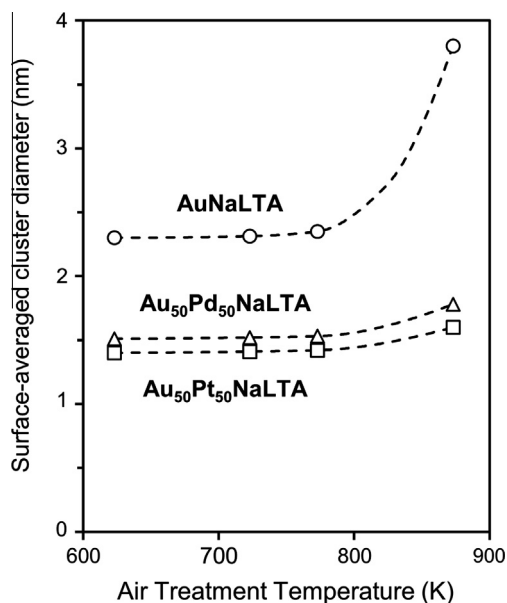


Fig. 3. Effects of the thermal treatment temperature in flowing dry air ($1.67 \text{ cm}^3 \text{ g}^{-1} \text{ s}^{-1}$, 0.033 K s^{-1} , 5 h) on the TEM-derived surface-averaged cluster diameter ($\langle d_{\text{TEM}} \rangle$, Eq. (1)) of metal particles in AuNaLTA (\circ), Au₅₀Pd₅₀NaLTA (\triangle), and Au₅₀Pt₅₀NaLTA (\square). The total metal content in each sample is $\sim 1\%$ wt.

frequency. Pt-CO bands are evident in each bimetallic sample spectrum both before and after intermittent heating in CO. The intensity of these bands increased monotonically with increasing Pt content, indicative of a concomitant increase in the Pt content of the cluster surfaces. A distinct Au-CO band is visible in the Au-rich bimetallic sample (Au₆₇Pt₃₃CaLTA) before and after heating in CO, but becomes weaker and ultimately undetectable at lower Au/Pt ratios. The weakening of this Au-CO band intensity is consistent with the decreasing overall Au content and the preferential adsorption of CO onto more strongly binding Pt atoms at bimetallic surfaces. Heating of Pt-Au bimetallic samples in CO led to hysteresis in their absorbance intensity, while the spectra for monometallic samples were unchanged. The intensity of Pt-CO bands in alloy samples increased after such heating cycles, reflecting the enrichment of Pt-Au particle surfaces with Pt as intracuster atomic mobility increases with increasing temperature. The fractional increase in the Pt-CO band intensity is smaller on samples with greater Pt/Au atomic ratios (20%, 15%, and 9% for Pt/Au = 0.5, 1, and 2, respectively), consistent with smaller changes in the fraction of exposed Pt atoms upon CO binding for clusters that are more dilute in Au. We conclude from this infrared evidence that both Pt and Au are present within the same clusters in all Au_nPt_{100-n}CaLTA samples.

3.3.2. Infrared spectra of chemisorbed CO on Au_nPd_{100-n}CaLTA

The infrared spectra of chemisorbed CO on 1% wt. Au_nPd_{100-n}CaLTA samples ($n = 0, 33, 50, 67, \text{ and } 100$) in 1.0 kPa

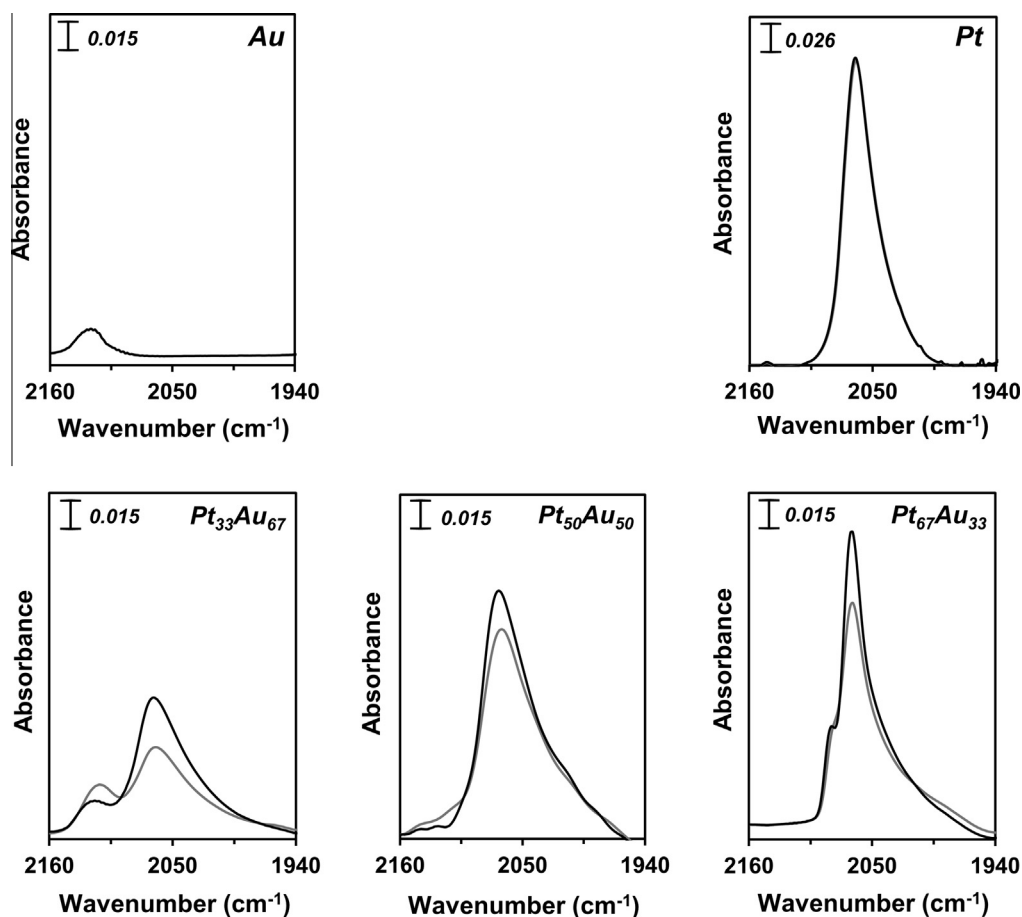


Fig. 4. Infrared spectra of CO adsorbed on monometallic or bimetallic Au_nPt_{100-n}CaLTA samples (1 kPa CO, 99 kPa He) at 263 K after H₂ treatment (573 K, 20 kPa H₂, 80 kPa He) (gray spectra) and after heating in CO (1 kPa CO, 99 kPa He) up to 353 K (black spectra).

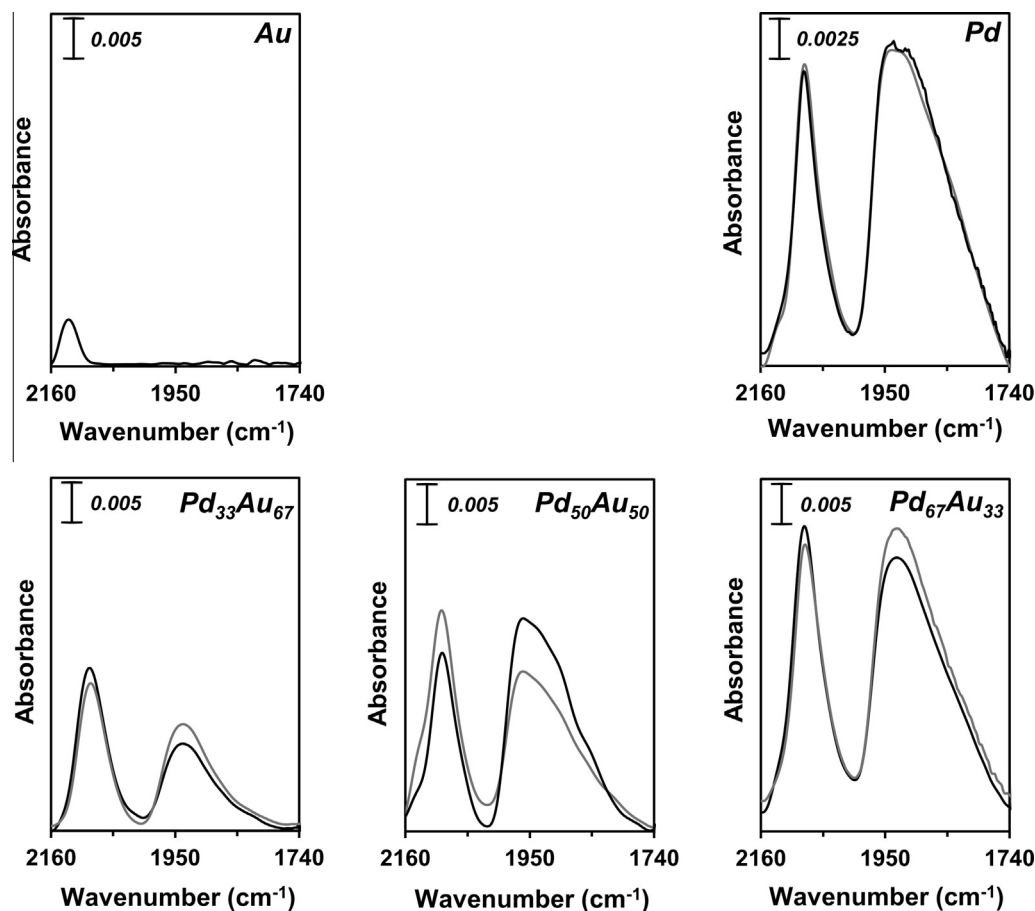


Fig. 5. Infrared spectra of CO adsorbed on monometallic or bimetallic Au_nPd_{100-n} CaLTA samples (1 kPa CO, 99 kPa He) at 278 K after H_2 treatment (573 K, 20 kPa H_2 , 80 kPa He) (gray spectra) and after heating in CO (1 kPa CO, 99 kPa He) up to 353 K (black spectra).

CO at 278 K before and after intervening treatments at 353 K are shown in Fig. 5. AuCaLTA shows a weak absorption band at 2130 cm^{-1} , corresponding to atop adsorption of CO on Au [14], while PdCaLTA shows much more intense bands at 2090 cm^{-1} and 1930 cm^{-1} , assigned to atop and bridged CO bound on Pd domains, respectively [42]. The weak Au-CO band reflects the prevailing low coverages at these conditions [43,44]. Atop and bridged Pd-CO bands are evident in all Au_nPd_{100-n} CaLTA spectra, but Au-CO bands cannot be clearly discerned because of their significant overlap with more intense atop Pd-CO bands. Pd-CO band intensities increased with increasing Pd/Au ratios, both before and after heating in CO, indicative of a concomitant increase in the Pd fraction at cluster surfaces. The ratio of the integrated intensities (I) of the bridged and atop Pd-CO bands ($\alpha = I_{\text{bridge}}/I_{\text{atop}}$) increased monotonically with increasing Pd content (Fig. 6). A preference for bridge-bonding, which requires multi-atom Pd ensembles, reflects a decrease in Au content at cluster surfaces. The α values for samples with separate Au and Pd clusters would resemble those on pure Pd and be unaffected by thermal treatments in CO, which favor intra-cluster surface segregation of Pd atoms only in bimetallic clusters. Figs. 5 and 6 show that the prevalence of bridge-bonded CO increases after exposure to CO at 353 K for Au_nPd_{100-n} CaLTA, but not for PdCaLTA samples. These data thus confirm the CO-induced surface segregation of Pd, which becomes possible only when the two components are present within the same cluster.

The spectra of CO adsorbed on monometallic Pd samples (Fig. 5) are similar to those reported in the literature, both in terms of their absorption frequencies (atop: 2090 cm^{-1} ; bridged: 1930 cm^{-1}) and the prevalent bridged CO binding ($\alpha = 2.4$) [9,39,40,42]. The

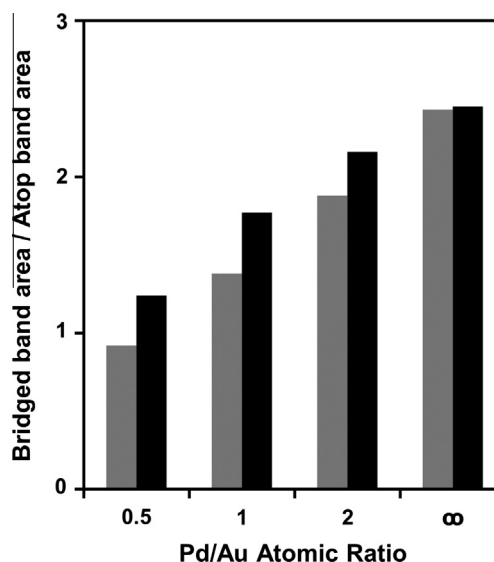


Fig. 6. Ratios of the integrated intensity of the Pd-CO (bridged) infrared absorption band to that of the Pd-CO atop band as a function of Pd/Au atomic ratio in Au_nPd_{100-n} CaLTA samples. Intensity ratios ($\alpha = I_{\text{bridge}}/I_{\text{atop}}$) calculated from spectra measured under 1 kPa CO at 278 K after H_2 treatment (573 K, 20 kPa H_2 , 80 kPa He) (gray bars) and after heating in CO (1 kPa CO, 99 kPa He) up to 353 K (black bars).

presence of adsorbed contaminants on the metal surfaces in PdCaLTA, such as residual sulfur species from the protecting ligands (Section 2.2), would have resulted in much less prevalent

bridged-bonded CO because of the requirement for multi-atom Pd ensembles and in much lower frequencies as a result of weaker dipole coupling. The presence of titrants on metal surfaces in PtCaLTA would have resulted in lower absorption frequencies than reported on clean Pt surfaces (2123–2054 cm^{-1} , [39,41]) and observed in the present study (2070 cm^{-1}). Sulfur contaminants would preferentially titrate Pt or Pd surface atoms because of the high bond energies of Pt-S (233 kJ mol^{-1} , [45]) and Pd-S (183 kJ mol^{-1} , [45]) relative to Au-S (126 kJ mol^{-1} , [46]). These sulfur species, if present, would have precluded the observed intra-cluster restructuring (Figs. 4 and 5), because S, with its stronger binding than CO, would have led to Pt or Pd segregation before exposure to CO(g) and thus prevented additional surface enrichment as a result of the temperature cycles. The clean nature of these bimetallic surfaces is consistent with chemisorption and infrared data for Pt, Pd, and Au clusters in LTA treated at similar conditions (air 623 K, H_2 623 K; Section 2.2) [13,14]. We conclude that the bimetallic clusters in $\text{Au}_n\text{Pd}_{100-n}\text{CaLTA}$ contain accessible surfaces free of synthetic debris.

3.3.3. Infrared spectra of chemisorbed CO on $\text{Pd}_n\text{Pt}_{100-n}\text{CaLTA}$

Fig. 7a shows the infrared spectra of CO chemisorbed on $\text{Pd}_n\text{Pt}_{100-n}\text{CaLTA}$ ($n = 100, 80, 65, 50, 20$, and 0) at 313 K and 1.0 kPa CO. On monometallic Pt and Pd samples, these spectra resemble those measured at lower temperatures (Pt-CO: 263 K, Fig. 4; Pd: 278 K, Fig. 5). PtCaLTA shows an intense band for atop CO binding at 2070 cm^{-1} , while PdCaLTA shows the characteristic Pd bands for atop (2090 cm^{-1}) and bridged (1930 cm^{-1}) CO. The presence of Pt leads to an increase in the intensity of atop CO bands that is monotonic with Pt content in $\text{Pd}_n\text{Pt}_{100-n}\text{CaLTA}$, together with a concomitant decrease in the bridged Pd-CO band intensity. The ratio of the integrated intensities for these bands ($\alpha = I_{\text{bridge}}/I_{\text{atop}}$) as a function of Pd content is shown in Fig. 7b. These trends indicate that surfaces become enriched with Pt as the Pt/Pd ratio increases, leading to a decrease in the size of Pd surface ensembles and thus to weaker features for bridge-bonded CO. The value of α declines from 2.8 to 0.1 as the Pd content is diluted from 100% to 50% at., and bridged Pd-CO bands are completely absent for samples with 20% at. Pd. Separate Pt and Pd clusters

would have had undiluted Pd ensembles even at very high Pt/Pd ratios, thus giving non-zero α values for all samples containing Pt. These data provide evidence for the prevalence of bimetallic particles in $\text{Pd}_n\text{Pt}_{100-n}\text{CaLTA}$ samples.

3.4. X-ray absorption fine structure spectra and the local structure and composition of clusters

The evidence presented up to this point for the presence of highly dispersed bimetallic clusters in $\text{Au}_n\text{Pd}_{100-n}\text{NaLTA}$, $\text{Au}_n\text{Pt}_{100-n}\text{NaLTA}$, and $\text{Pd}_n\text{Pt}_{100-n}\text{NaLTA}$ has been based on particle size distributions (Section 3.2), thermal stability (Section 3.2), and on the infrared spectra of chemisorbed CO (Section 3.3). Such data, taken together, are compelling but remain indirect and plausibly circumstantial. The bimetallic clusters are small (1.3–1.7 nm; Table 1) and uniform in size (DI 1.05–1.15; Table 1), an observation inconsistent with clusters heterogeneous in composition, which would have shown a broad range of cluster sizes (i.e. DI > 1.5, [17]) reflecting their different thermal stabilities. The addition of Pd or Pt to Au stabilizes the lower-melting Au clusters against sintering (Fig. 3), consistent with heteroatomic metal bonding that is stronger than the like-metal bonding that prevails in monometallic clusters of the less stable metal [31]. The marked hysteresis in the infrared spectra (Section 3.3), evident upon heating to induce intra-cluster rearrangements (AuPt, Section 3.3.1; AuPd, Section 3.3.2), and the selective decrease in bridge-bonded CO upon addition of Pt to Pd (PdPt, Section 3.3.3), are inconsistent with mixtures of predominantly monometallic clusters. None of these techniques, however, provides direct quantitative evidence of the extent to which the two metals have mixed within a given cluster.

Energy dispersive X-ray spectroscopy (EDS) techniques allow detailed particle-by-particle elemental analysis in many scenarios [47], but elemental mapping of the very small clusters in this study would require electron currents or acquisition times that severely damage both metal structures and zeolite crystals [47,48]. As a result, we have used instead X-ray absorption spectroscopy (XAS) to probe the extent of metal mixing in bimetallic samples. In this section, we provide XAS results with a detailed analysis of the extended fine structure (EXAFS) region for $\text{Au}_{50}\text{Pd}_{50}\text{NaLTA}$ and

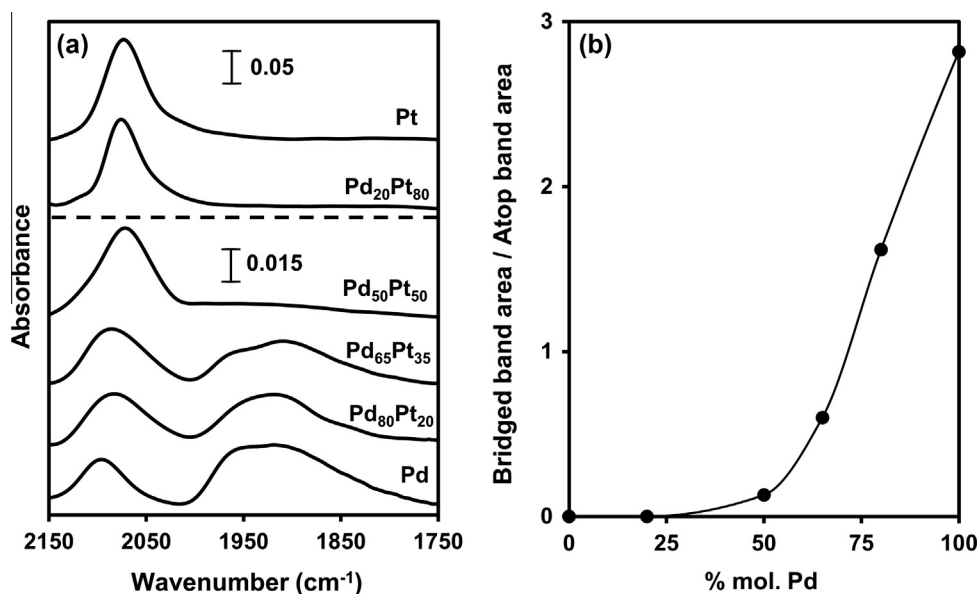


Fig. 7. (a) Infrared spectra of CO adsorbed on monometallic or bimetallic $\text{Pd}_n\text{Pt}_{100-n}\text{CaLTA}$ samples (1 kPa CO, 99 kPa He) at 313 K after H_2 treatment (573 K, 20 kPa H_2 , 80 kPa He). (b) Ratio of the integrated intensity of the Pd-CO (bridged) absorption band ($\sim 1900 \text{ cm}^{-1}$) to that of the metal-CO atop band ($\sim 2100 \text{ cm}^{-1}$) as a function of Pd content in $\text{Pd}_n\text{Pt}_{100-n}\text{CaLTA}$ samples.

Pd₆₅Pt₃₅NaLTA samples in order to determine the number and composition of the atoms surrounding each absorber element; these data confirm the small size and the compositional uniformity of the bimetallic samples prepared by the procedures reported here.

The k^3 -weighted and Fourier transformed EXAFS data with their respective regressed fits are shown for bimetallic samples and reference foils at the Au-L₃, Pd-K, and Pt-L₃ edges in Figs. 8–10, respectively. XAS spectra for these samples, including near-edge and post-edge data before data processing, are included in the SI (Figs. S2 and S3). Also included in the SI are the k^2 -weighted EXAFS data prior to the application of Fourier transformations (Figs. S4 and S5). The coordination numbers (N), interatomic distances (D), and Debye–Waller factors (σ^2) obtained from the regression of the EXAFS data using single scattering methods are reported in Table 2.

3.4.1. EXAFS analysis of Au₅₀Pd₅₀NaLTA spectra

Fig. 8 shows the Fourier transform amplitudes and the corresponding regression fits of the EXAFS oscillations at the Au-L₃ edge for Au₅₀Pd₅₀NaLTA and the Au foil. The fits of the Au-L₃ EXAFS for Au₅₀Pd₅₀NaLTA confirm that Au absorbers are coordinated with both Au and Pd atoms, with Au–Au and Au–Pd coordination numbers ($N_{\text{Au–Au}}$, $N_{\text{Au–Pd}}$) of 6 ± 1 and 3.2 ± 0.8 at distances of $2.73 \pm 0.02 \text{ \AA}$ and $2.73 \pm 0.01 \text{ \AA}$, respectively (Table 2). The first Au coordination shell thus contains a total of 9 ± 1 atoms after appropriate propagation of uncertainties [49]. This total coordination number is much smaller than the value of 12 characteristic of large Au or AuPd crystals [22], indicating the prevalence of coordinatively unsaturated surface atoms in highly dispersed clusters. The Au–Pd interatomic distance (2.73 \AA) derived from the fit is also smaller than that of a bulk Au₅₀Pd₅₀ alloy ($\sim 2.81 \text{ \AA}$) [22], consistent with the demonstrated contraction of metal–metal bonds near cluster surfaces [50]. The total coordination number (9 ± 1) is compatible with an fcc cubooctahedral cluster with diameter between 1.3 and 2.1 nm [50–53]; this diameter is in agreement with that measured by TEM (1.6 nm) (Table 1).

Next, we compare these results with those extracted from the EXAFS signal at the Pd-K edge to confirm their internal consistency. Fourier transform amplitudes and fits of the EXAFS oscillations at

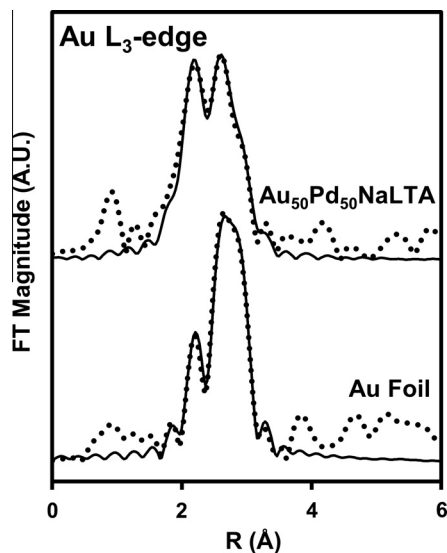


Fig. 8. Fourier transforms (FT) of the k^3 -weighted EXAFS and their corresponding single scattering fits for Au_nPd_{100–n}NaLTA and Au foil measured at the Au-L₃ edge. Dotted lines, experimental data; solid lines, fitted data. X-ray absorption spectra were collected at ambient temperature under 100 kPa Ar following H₂ treatment (573 K, 10 kPa H₂, 90 kPa He).

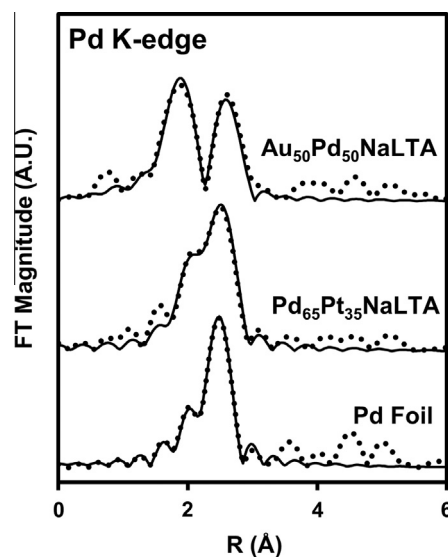


Fig. 9. Fourier transforms (FT) of the k^3 -weighted EXAFS and their corresponding single scattering fits for Au₅₀Pd₅₀NaLTA, Pd₆₅Pt₃₅NaLTA, and Pd foil measured at the Pd-K edge. Dotted lines, experimental data; solid lines, fitted data. X-ray absorption spectra were collected at ambient temperature under 100 kPa Ar following H₂ treatment (573 K, 10 kPa H₂, 90 kPa He).

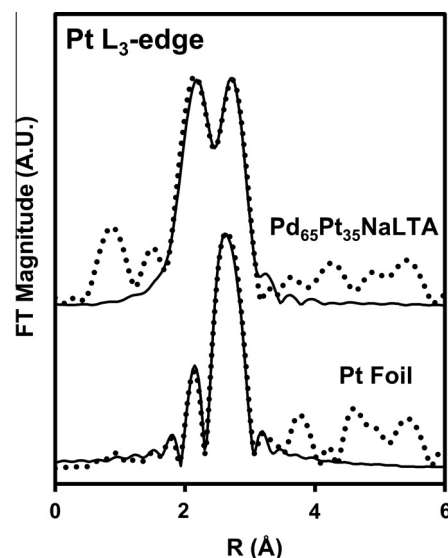


Fig. 10. Fourier transforms (FT) of the k^3 -weighted EXAFS and their corresponding single scattering fits for Pd₆₅Pt₃₅NaLTA and Pt foil measured at the Pt-L₃ edge. Dotted lines, experimental data; solid lines, fitted data. X-ray absorption spectra were collected at ambient temperature under 100 kPa Ar following H₂ treatment (573 K, 10 kPa H₂, 90 kPa He).

the Pd-K edge for Au₅₀Pd₅₀NaLTA and Pd foil are shown in Fig. 9. Structural parameters derived from these fits (Table 2) show that both Au and Pd are coordinated to the Pd absorbers, with a Pd–Pd coordination number of 3.1 ± 0.7 at a distance of $2.69 \pm 0.01 \text{ \AA}$ and a Pd–Au coordination number of 5 ± 1 at a distance of $2.73 \pm 0.01 \text{ \AA}$. These individual coordination numbers give a total Pd coordination of 8 ± 1 . Fits at the Au-L₃ and Pd-K edges did not reveal any metal–S or metal–O coordination, consistent with the exclusive presence of metallic phases. The total coordination numbers for Au and Pd absorbers are similar within the experimental uncertainty, as are the heteroatomic coordination numbers calculated at each metal edge (i.e. $N_{\text{Au–Pd}}$ and $N_{\text{Pd–Au}}$), indicating that the Au and Pd atoms occupy clusters with similarly high dispersion

Table 2

Coordination numbers, interatomic distances, and Debye–Waller factors derived from single scattering fits of the EXAFS spectra for the zeolite-encapsulated bimetallic nanoparticles.

Sample	Edge	Scatterer	N^a	D (Å) ^b	σ^2 (Å ²) ^c
Au ₅₀ Pd ₅₀ NaLTA	Au-L ₃	Au	6 (1)	2.73 (2)	0.011 (4)
		Pd	3.2 (8)	2.73 (1)	0.008 (2)
	Pd-K	Au	5 (1)	2.73 (1)	0.008 (2)
		Pd	3.1 (7)	2.69 (1)	0.007 (1)
Pd ₆₅ Pt ₃₅ NaLTA	Pd-K	Pd	4.4 (4)	2.74 (1)	0.008 (1)
		Pt	4.0 (3)	2.73 (1)	0.008 (1)
	Pt-L ₃	Pd	4 (1)	2.73 (1)	0.008 (1)
		Pt	5 (1)	2.72 (1)	0.008 (1)

^a Average coordination number of absorbing element.

^b Interatomic distance.

^c Debye–Waller factor. Values in parentheses indicate the error in the last digit.

and are in intimate contact within clusters that must therefore contain both elements. The mean atomic coordination between unlike atoms (4 ± 1), computed as the average of $N_{\text{Au-Pd}}$ and $N_{\text{Pd-Au}}$, is approximately half the average total coordination (9 ± 1), indicating that bonds between unlike atoms are equally prevalent as homoatomic bonds. Such similar numbers of homoatomic and heteroatomic bonds are consistent with all clusters reflecting the bulk equimolar amounts of the two elements ($\text{Pd/Au} = 1$), with the absence of segregated metal phases, and with essentially uniform distributions of each metal atom within each cluster. Surface enrichment of Au brought forth by pretreatment of the sample (H_2 , 353 K; Section 3.3) would have resulted in a slight preference for homoatomic bonds; such intracuster segregation was either lost during the intervening period between treatments and XAS spectra acquisition (Section 2.3.4) or could not be accurately detected by the single scattering models used here. These parameters derived from the EXAFS, however, are consistent at each metal edge and confirm the small size and intimate metal mixing in Au₅₀Pd₅₀NaLTA, as well as the substantial absence of monometallic clusters.

3.4.2. EXAFS analysis of Pd₆₅Pt₃₅NaLTA spectra

Fig. 9 shows the Fourier transform amplitudes and fits of the EXAFS signal at the Pd-K edge of Pd₆₅Pt₃₅NaLTA; structural parameters derived from these fits are shown in Table 2. Pd absorbers were coordinated to both Pd and Pt atoms with coordination numbers of 4.4 ± 0.4 and 4.0 ± 0.3 at distances of 2.74 ± 0.01 and 2.73 ± 0.01 Å, respectively. These coordination shells lead to a total Pd atom coordination of 8.4 ± 0.5 , compatible with 1.1–1.7 nm diameter clusters with an fcc cuboctahedral structure [50–53], in good agreement with the mean cluster size determined from TEM images (1.2 nm, Table 2).

Fig. 10 shows the corresponding Fourier transform amplitudes and fits of the EXAFS at the Pt-L₃ edge of Pd₆₅Pt₃₅NaLTA. Structural parameters extracted from the fit (Table 2) show that Pt absorbers are coordinated to both Pt and Pd atoms, with Pt–Pt and Pt–Pd coordination numbers ($N_{\text{Pt-Pt}}$, $N_{\text{Pt-Pd}}$) of 5 ± 1 and 4 ± 1 at distances 2.72 ± 0.01 Å and 2.73 ± 0.01 Å, respectively. Pt absorbers thus contain a total of 9 ± 1 atoms in their first coordination shell. This total coordination number is similar to the total coordination derived for Pd atoms (8.4 ± 0.5), indicating that the Pd and Pt atoms occupy clusters with a large and similar fraction of coordinatively unsaturated surface atoms. Pd and Pt absorbers did not show any metal–S or metal–O coordination, consistent with the presence of only metallic phases. PdPt clusters with the bulk composition of Pd₆₅Pt₃₅NaLTA (61 Pd: 39 Pt, Table 1), a total coordination of 9 ± 1 , and random intracuster locations of Pt and Pd would exhibit Pd–Pt and Pt–Pd coordination numbers ($N_{\text{Pd-Pt}}$ and $N_{\text{Pt-Pd}}$) of 4 and 5, respectively, which agree within experimental uncertainty with

those derived from EXAFS data; thus, we conclude that clusters are uniform in composition and contain random intracuster distributions of two elements. The prevalence of Pt-rich or Pd-rich clusters would have led to smaller $N_{\text{Pd-Pt}}$ and $N_{\text{Pt-Pd}}$ values than expected for clusters of uniform composition.

3.5. Ethanol oxidative dehydrogenation rates and titration of extracrystalline surfaces by large organosulfur poisons as a probe of encapsulation selectivity

Metal cluster confinement within zeolites precludes certain reactants or poisons from accessing intracrystalline clusters; such restricted access also serves to retain large products until they convert to smaller species that can egress by diffusion, while the small intracrystalline voids can stabilize specific transition states. In all cases, these effects are dictated by the size of the voids and their connecting apertures in a given microporous framework [13–15]. Here, we exploit such zeolite shape selective properties by measuring oxidative dehydrogenation (ODH) turnover rates of a small molecule (ethanol, 0.40 nm kinetic diameter, [13]) on samples exposed to a large organosulfur molecule that poisons metal surfaces (dibenzothiophene, DBT; 0.9 nm, [30]) to estimate the extent to which bimetallic clusters reside within zeolite crystals. Organosulfur compounds such as DBT irreversibly adsorb onto Au, Pd, and Pt surfaces, forming unreactive species that block active sites [29]. Consequently, ethanol ODH turnover rates on metal–SiO₂ samples and extracrystalline bimetallic clusters in metal–NaLTA samples would be suppressed by DBT, while clusters protected by the small NaLTA apertures (0.42 nm, [13]) would retain their ODH rates because they cannot be reached by DBT. The rate differences upon contact with DBT then provide a measure of the selectivity of metal encapsulation within intracrystalline domains.

Alkanol ODH reactions form alkanals as primary products; these alkanals can undergo subsequent reactions with alkanols to form hemiacetals or alkoxyalkanols and then dialkoxyalkanes and carboxylic acids through secondary dehydrogenation, oxidation, or condensation reactions [54,55]. These secondary reactions do not affect measured turnover rates, because each product molecule formed involves a single ODH event, in which an alkanal forms via kinetically-relevant β -H abstraction from an adsorbed alkoxide by chemisorbed oxygen [14,55]. The low conversions prevalent in this study (<5%) minimize secondary reactions and lead to high acetaldehyde selectivities (>95%, C-basis).

Samples were exposed to DBT as described in Section 2.3.5 before ODH rate measurements at 393 K. ODH rates were also measured on samples that were not contacted with DBT (denoted as “control samples”), but treated otherwise identically. ODH turnover rates measured on these controls (r_{ODH}) and on samples exposed to DBT ($r_{\text{ODH,DBT}}$) are used to define a parameter Λ_{DBT} :

$$\Lambda_{\text{DBT},i} = \frac{r_{\text{ODH,DBT}}}{r_{\text{ODH}}} \quad (4)$$

where i identifies the specific sample (e.g., Au₅₀Pd₅₀NaLTA, Pt/SiO₂). The value of $\Lambda_{\text{DBT},i}$ reflects the fraction of the active surfaces that remain active for ODH after DBT exposure. A $\Lambda_{\text{DBT},i}$ value of unity would reflect fully protected clusters, while a value of zero would indicate that all active surfaces can be accessed and fully poisoned by DBT. Metal clusters encapsulated within LTA crystals would be inaccessible to DBT and thus protected from deactivation, while metal clusters outside the zeolite crystals should be accessible and deactivated by DBT. Exposure to DBT thus selectively suppresses the contributions to the ODH rate from extrazeolite clusters. As a result, the value of $\Lambda_{\text{DBT},i}$ is proportional to the fraction of encapsulated clusters in metal–zeolite samples. Values of r_{ODH} and $\Lambda_{\text{DBT},i}$ for Au, Pd, and Pt clusters supported on mesoporous SiO₂

Table 3
Rates of ethanol oxidative dehydrogenation on metal-SiO₂ and metal-NaLTA samples.

Sample	r_{ODH} ($10^{-3} \text{ s}^{-1} \text{ mol}_{\text{surf-metal}}^{-1}$) ^a	Λ_{DBT} ^b
Au ₅₀ Pd ₅₀ NaLTA	110	0.97
Au ₅₀ Pt ₅₀ NaLTA	210	0.95
Pd ₆₅ Pt ₃₅ NaLTA	280	0.98
Au/SiO ₂	12	0.11
Pd/SiO ₂	320	0.03
Pt/SiO ₂	490	0.04

^a Ethanol ODH turnover rates of samples agitated in EtOH (300 cm³ g⁻¹) at ambient temperature for 4 h, treated in ambient air at 343 K for 12 h, then used in reaction (393 K under 9 kPa O₂, 4 kPa EtOH, and 0.5 kPa H₂O).

^b $r_{\text{ODH,DBT}}/r_{\text{ODH}}$ (Eq. (4)), where $r_{\text{ODH,DBT}}$ is the ethanol ODH rate of analogously treated samples but with DBT dissolved in the EtOH at a 6:1 DBT:metal molar ratio. Reaction turnover rate defined as number of moles of reactant converted per time normalized by the number of exposed surface metal atoms estimated by TEM (Eq. (3)).

and a representative group of bimetallic samples are shown in Table 3.

Ethanol ODH turnover rates were much more weakly suppressed by contact with DBT on metal-NaLTA ($\Lambda_{\text{DBT},i} = 0.95 - 0.98$) than on metal-SiO₂ ($\Lambda_{\text{DBT},i} = 0.03 - 0.11$) samples (Table 3), indicating that (i) DBT effectively titrates unprotected noble metal surfaces; and (ii) most of the metal clusters reside within LTA crystals in metal-NaLTA samples. The small residual ODH activity on SiO₂-supported samples, even after contact with excess DBT (6:1 DBT:metal molar ratio), may reflect steric effects that hinder access to remaining open sites as DBT-derived species reach near-saturation coverages [38]. The remarkable resistance to DBT poisoning in metal-NaLTA samples, evident in their $\Lambda_{\text{DBT},i}$ values near unity (0.95–0.98) (Table 3), provides compelling evidence for the near complete encapsulation of these bimetallic clusters, as also found for monometallic clusters encapsulated within LTA and other zeolites using similar hydrothermal synthesis protocols [13,14]. Such resistance may also prove useful in practice when poisons larger than the reactants and products of interest are present in reacting streams.

We therefore conclude that the hydrothermal encapsulation method described here can be more generally applied to prepare bimetallic clusters which are small and uniform in size (Section 3.2), highly stable against thermal sintering (Section 3.2), homogeneously distributed in composition (Sections 3.3 and 3.4), and selectively encapsulated within zeolite crystals (Section 3.5).

4. Conclusion

A general procedure was developed for the encapsulation of highly dispersed bimetallic clusters (1–2 nm), uniformly distributed in size and composition, within the voids of the LTA zeolite using a ligand-assisted hydrothermal synthesis technique. Samples with AuPd, AuPt, and PdPt clusters and a variety of metal compositions were synthesized to demonstrate the broad applicability of the technique. Metal encapsulation and alloying is conferred by introducing mercaptosilane-stabilized metal cation precursors into zeolite synthesis gels, which are crystallized hydrothermally to form LTA with metal cations occluded in the pores. The anchoring of these ligated cations to the zeolite framework via siloxane bridges enforces their uniform dispersion throughout the zeolite crystals. Treatment of the crystallized zeolites in O₂ and then H₂ forms bimetallic clusters, which remain narrowly distributed in size following oxidative treatments in excess of 773 K. Such thermal stability results from the confinement of the metal clusters within microporous zeolite voids, which impose thermodynamic barriers that inhibit cluster growth. Encapsulated Au metal further benefits from enhanced thermal sinter-stability

through alloying with higher-melting Pd or Pt metal. Metal confinement also exploits the catalytic shape-selective properties of zeolites, which act to protect active metal surfaces from contact by large poison molecules. The present work outlines the synthesis of bimetallic clusters of well-defined size and composition, allowing rigorous studies of alloyed nanoparticle catalysts even at conditions which strongly favor metal agglomeration. Such studies may combine the well-known reactant size selection properties of small-pore zeolites with the synergistic catalysis of bimetallic clusters for tailored applications of these materials. The successful application of this technique to a variety of metal pairs and compositions leads us to predict that it can be analogously applied to any combination of metals (Au, Pd, Pt, Ir, Ag, Rh) and zeolites (LTA, MFI) for which monometallic hydrothermal encapsulation techniques have been developed.

Author contributions

T.O., S.I.Z., and E.I. conceived and developed the synthesis technique, and drafted most of the manuscript. J.M.R.-L., L.G., and F.G.R. conducted XAS experiments, processed the XAS data with the IFEFFIT package, assisted in the interpretation of EXAFS data, and wrote the description of the XAS methods and data. T.O. performed all chemical syntheses and the other characterization experiments, including the catalytic experiments.

Notes

The authors declare the following competing financial interest (s): (1) The funding for a significant portion of this research was provided by the Chevron Energy Technology Co., and (2) Stacey I. Zones is an employee of this company and, more generally, also a stockholder of the Chevron Corp.

Acknowledgments

We gratefully acknowledge the generous financial support of the Chevron Energy Technology Co, as well as ancillary research support from CONICET (PIP No. 1035) and LNLS (Project XAFS1-18861) and an ARCS Foundation Fellowship (for TO). We thank Dr. Reena Zalpuri (Electron Microscope Lab) for support with TEM instrumentation and Dr. Antonio DiPasquale (X-Ray Facility) for assistance with the acquisition of diffraction data.

Appendix A. Supplementary material

Supplementary data associated with this article can be found, in the online version, at <http://dx.doi.org/10.1016/j.jcat.2016.07.017>.

References

- [1] W.-Y. Yu, L. Zhang, G.M. Mullen, G. Henkelman, C.B. Mullins, Oxygen activation and reaction on Pd-Au bimetallic surfaces, *J. Phys. Chem. C* 119 (2015) 11754–11762.
- [2] J.C. Serrano-Ruiz, A. Sepúlveda-Escribano, F. Rodríguez-Reinoso, Bimetallic PtSn/C catalysts promoted by ceria: application in the nonoxidative dehydrogenation of isobutane, *J. Catal.* 246 (2007) 158–165.
- [3] R.M. Wolf, J. Siera, F. Vandelft, B.E. Nieuwenhuys, A comparative study of the behaviour of single-crystal surfaces and supported catalysts in NO reduction and CO oxidation over Pt-Rh alloys, *Faraday Discuss. Chem. Soc.* 87 (1989) 275–289.
- [4] G. Riah, D. Guillemot, M. Polisset-Thfoin, A.A. Khodadadi, J. Fraissard, Preparation, characterization and catalytic activity of gold-based nanoparticles on HY zeolites, *Catal. Today* 72 (2002) 115–121.
- [5] Z. Zhang, W.M.H. Sachtler, S.L. Suib, Proximity requirement for Pd enhanced reducibility of Co²⁺ in NaY, *Catal. Lett.* 2 (1989) 395–402.
- [6] T. Rades, C. Pak, M. Polisset-Thfoin, R. Ryoo, J. Fraissard, Characterization of bimetallic NaY-supported Pt-Pd catalyst by EXAFS, TEM and TPR, *Catal. Lett.* 29 (1994) 91–103.

- [7] T. Wada, K. Kaneda, S. Murata, M. Nomura, Effect of modifier Pd metal on hydrocracking of polyaromatic compounds over Ni-loaded Y-type zeolite and its application as hydrodesulfurization catalyst, *Catal. Today* 31 (1996) 113–120.
- [8] Z. Paál, A. Wootsch, D. Teschner, K. Lázár, I.E. Sajó, N. Gyórfy, G. Weinberg, A. Knop-Gericke, R. Schlögl, Structural properties of an unsupported model Pt-Sn catalyst and its catalytic properties in cyclohexene transformation, *Appl. Catal. A* 391 (2011) 377–385.
- [9] S. Kunz, E. Iglesia, Mechanistic evidence for sequential displacement–reduction routes in the synthesis of Pd-Au clusters with uniform size and clean surfaces, *J. Phys. Chem. C* 118 (2014) 7468–7479.
- [10] O.S. Alexeev, B.C. Gates, Supported bimetallic cluster catalysts, *Ind. Eng. Chem. Res.* 42 (2003) 1571–1587.
- [11] J. Rebelli, A.A. Rodriguez, S. Ma, C.T. Williams, J.R. Monnier, Preparation and characterization of silica-supported, group 1B-Pd bimetallic catalysts prepared by electrodeless deposition methods, *Catal. Today* 160 (2011) 170–178.
- [12] S. Alayoglu, P. Zavalij, B. Eichhorn, Q. Wang, A.I. Frenkel, P. Chupas, Structural and architectural evaluation of bimetallic nanoparticles: a case study of Pt–Ru core–shell and alloy nanoparticles, *ACS Nano* 3 (2009) 3127–3137.
- [13] M. Choi, Z. Wu, E. Iglesia, Mercaptosilane-assisted synthesis of metal clusters within zeolites and catalytic consequences of encapsulation, *J. Am. Chem. Soc.* 132 (2010) 9129–9137.
- [14] T. Otto, S.I. Zones, E. Iglesia, Challenges and strategies in the encapsulation and stabilization of monodisperse Au clusters within zeolites, *J. Catal.* 339 (2016) 195–208.
- [15] P.B. Weisz, V.J. Frilette, R.W. Maatman, E.B. Mower, Catalysis by crystalline aluminosilicates II. Molecular–shape selective reactions, *J. Catal.* 1 (1962) 307–312.
- [16] H. Zhu, Z. Ma, J.C. Clark, Z. Pan, S.H. Overbury, S. Dai, Low-temperature CO oxidation on Au/fumed SiO₂-based catalysts prepared from Au(en)₂Cl₃ precursor, *Appl. Catal. A* 326 (2007) 89–99.
- [17] G. Bergeret, P. Gallezot, in: G. Ertl, H. Knozinger, F. Schuth, J. Weitkamp (Eds.), *Handbook of Heterogeneous Catalysis*, Weinheim, Germany, Wiley-VCH, 2008, pp. 738–765.
- [18] J.A. Bearden, X-ray wavelengths, *Rev. Mod. Phys.* 39 (1967) 78–124.
- [19] B. Ravel, M. Newville, ATHENA, ARTEMIS, HEPHAESTUS: data analysis for X-Ray absorption spectroscopy using IFEFFIT, *J. Synchrotron Rad.* 12 (2005) 537–541.
- [20] S.I. Zabinsky, J.J. Rehr, A. Ankudinov, R.C. Albers, M.J. Eller, Multiple-scattering calculations of X-ray-absorption spectra, *Phys. Rev. B* 52 (1995) 2995–3009.
- [21] S.M. Foiles, M.I. Baskes, M.S. Daw, Embedded-atom-method functions for the fcc metals Cu, Ag, Au, Ni, Pd, Pt, and their alloys, *Phys. Rev. B* 33 (1986) 7983–7991.
- [22] Y.C. Venudhar, L. Lyengar, K.V.K. Rao, X-Ray determination of the effect of temperature on the lattice parameters and the coefficients of thermal expansion of palladium–silver–gold alloys, *J. Less-Common Met.* 58 (1978) P55–P60.
- [23] E. Raub, G. Woerwag, Die gold-platin und palladium legierungen, *Z. Metallk.* 46 (1955) 513–515.
- [24] J. Waser, H.A. Levy, S.W. Peterson, The structure of PdO, *Acta Crystallogr.* 6 (1953) 661–663.
- [25] H.R. Hoekstra, S. Siegel, F.X. Gallagher, Reaction of platinum dioxide with some metal oxides, *Adv. Chem. Ser.* 98 (1971) 39–53.
- [26] N.E. Brese, P.J. Squattrito, J.A. Ibers, Reinvestigation of the structure of PdS, *Acta Crystallogr. C* 41 (1985) 1829–1830.
- [27] F.A. Bannister, M.H. Hey, Determination of minerals in platinum concentrates from the transval by X-Ray methods, *Mineral Mag. J. Mineral. Soc.* 23 (1932) 188–206.
- [28] T. Isonaga, K. Ishikawa, S. Wakita, Y. Suzuki, Structure and electrical properties of Au₂S, *Solid State Ionics* 79 (1995) 60–66.
- [29] E.O. Sako, H. Kondoh, I. Nakai, A. Nambu, T. Nakamura, T. Ohta, Reactive adsorption of thiophene on Au(111) from solution, *Chem. Phys. Lett.* 413 (2005) 267–271.
- [30] B. Van de Voorde, M. Hezino, J. Lannoeye, A. Vandekerckhove, B. Marszalek, B. Gil, I. Beurroies, P. Nachtiqall, D. De Vos, Adsorptive desulfurization with CPO-27/MOF-74: an experimental and computational investigation, *Phys. Chem. Chem. Phys.* 17 (2015) 10759–10766.
- [31] A. Cao, R. Lu, G. Veser, Stabilizing metal nanoparticles for heterogeneous catalysis, *Phys. Chem. Chem. Phys.* 12 (2010) 13499–13510.
- [32] S. Peng, J.M. McMahon, G.C. Schatz, S.K. Gray, Y. Sun, Reversing the size-dependence of surface plasmon resonances, *Proc. Natl. Acad. Sci. USA* 107 (2010) 14530–14534.
- [33] M. Sankar, N. Dimitratos, P.J. Miedziak, P.P. Wells, C.J. Kiely, G.J. Hutchings, Designing bimetallic catalysts for a green and sustainable future, *Chem. Soc. Rev.* 41 (2012) 8099–8139.
- [34] S. Kaya, E. Erunal, R. Shaltaf, Ş. Ellialtıođlu, D. Üner, On the structure sensitivity of CO oxidation on alumina supported Pd-Pt bimetallic catalysts, *Turk. J. Chem.* 33 (2009) 11–21.
- [35] C.W. Han, P. Majumdar, E.E. Marinero, A. Aguilar-Tapia, R. Zanella, J. Greeley, V. Ortolan, Highly stable bimetallic AuIr/TiO₂ catalyst: physical origins of the intrinsic high stability against sintering, *Nano Lett.* 15 (2015) 8141–8147.
- [36] A.R. Miedema, Surface energies of solid metals, *Z. Metallk.* 69 (1978) 287–292.
- [37] G.W. Smith, E.A. Carter, Interactions of NO and CO with Pd and Pt atoms, *J. Phys. Chem.* 95 (1991) 2327–2339.
- [38] R. Meyer, C. Lemire, S.K. Shaikhutdinov, H.-J. Freund, Surface chemistry of catalysis by gold, *Gold Bull.* 37 (2004) 72–124.
- [39] J. Lu, K.-B. Low, Y. Lei, J.A. Libera, A. Nicholls, P.C. Stair, J.W. Elam, Toward atomically-precise synthesis of supported bimetallic nanoparticles using atomic layer deposition, *Nat. Commun.* 5 (2014) 3264–3273.
- [40] O. Rosseleer, C. Ulhaq-Bouillet, A. Bonnefont, S. Pronkin, E. Savinova, A. Louvet, V. Keller, N. Keller, Structural and electronic effects in bimetallic PdPt nanoparticles on TiO₂ for improved photocatalytic oxidation of CO in the presence of humidity, *Appl. Catal. B* 166–167 (2015) 381–392.
- [41] Y. Barshad, X. Zhou, E. Gulari, Carbon monoxide oxidation under transient conditions: a fourier-transform infrared transmission spectroscopy study, *J. Catal.* 94 (1985) 128–141.
- [42] D. Stacchiola, M. Kaltchev, G. Wu, W.T. Tysoe, The adsorption and structure of carbon monoxide on ethylidyne-covered Pd(111), *Surf. Sci.* 470 (2000) L32–L38.
- [43] S. Derrouiche, P. Gravejat, D. Bianchi, Heats of adsorption of linear CO species adsorbed on the Au⁰ and Ti³⁺ sites of a 1% Au/TiO₂ catalyst using in situ FTIR spectroscopy under adsorption equilibrium, *J. Am. Chem. Soc.* 126 (2004) 13010–13015.
- [44] F. Menegazzo, M. Manzoli, A. Chiorino, F. Boccuzzi, T. Tabakova, M. Signoretto, F. Pinna, N. Pernicone, Quantitative determination of gold active sites by chemisorption and by infrared measurements of adsorbed CO, *J. Catal.* 237 (2006) 431–434.
- [45] H. Toulhoat, P. Raybaud, S. Kasztelan, G. Kresse, J. Hafner, Transition metals to sulfur binding energies relationship to catalytic activities in HDS: back to Sabatier with first principle calculations, *Catal. Today* 50 (1999) 629–636.
- [46] R.G. Nuzzo, F.A. Fusco, D.L. Allara, Spontaneously organized molecular assemblies. 3. Preparation and properties of solution adsorbed monolayers of organic disulfides on gold surfaces, *J. Am. Chem. Soc.* 109 (1987) 2358–2368.
- [47] A.A. Herzing, M. Wantanabe, J.K. Edwards, M. Conte, Z.R. Tang, G.J. Hutchings, C.J. Kiely, Energy dispersive X-ray spectroscopy of bimetallic nanoparticles in an aberration corrected scanning transmission electron microscope, *Faraday Discuss.* 138 (2008) 337–351.
- [48] O. Ugurlu, J. Haus, A.A. Gunawan, M.G. Thomas, S. Maheshwari, M. Tsapatsis, K. A. Mkhoyan, Radiolysis to knock-on damage transition in zeolites under electron beam irradiation, *Phys. Rev. B* 83 (2011) 113408.
- [49] J.R. Taylor, *An Introduction to Error Analysis, the Study of Uncertainties in Physical Measurements*, second ed., University Science Books, Sausalito, United States, 1997.
- [50] C. Mottet, G. Tréglia, B. Legrand, New magic numbers in metallic clusters: an unexpected metal dependence, *Surf. Sci.* 383 (1997) L719–L727.
- [51] A. Jentys, Estimation of mean size and shape of small metal particles by EXAFS, *Phys. Chem. Chem. Phys.* 1 (1999) 4059–4063.
- [52] A.I. Frenkel, C.W. Hills, R.G. Nuzzo, A view from the inside: complexity in the atomic scale ordering of supported metal nanoparticles, *J. Phys. Chem. B* 105 (2001) 12689–12703.
- [53] J.M. Ramallo-López, F.G. Requejo, A.F. Craievich, J. Wei, M. Avalos-Borja, E. Iglesia, Complementary methods for cluster size distribution measurements: supported platinum nanoclusters in methane reforming catalysts, *J. Mol. Catal.* 228 (2005) 299–307.
- [54] H. Liu, E. Iglesia, Selective oxidation of methanol on supported ruthenium oxide clusters at low temperatures, *J. Phys. Chem. B* 109 (2005) 2155–2163.
- [55] C. Louis, J.M. Tatibout, M. Che, Catalytic properties of silica-supported molybdenum catalysts in methanol oxidation: the influence of molybdenum dispersion, *J. Catal.* 109 (1988) 354–366.